

Changes in the mechanical environment of stenotic arteries during interaction with stents: computational assessment of parametric stent designs

Gerhard A. Holzapfel¹ and Michael Stadler

Institute for Structural Analysis – Computational Biomechanics

Graz University of Technology, 8010 Graz, Schiesstattgasse 14-B, Austria

Abstract. Clinical studies have identified factors such as the stent design and the deployment technique that are one cause for the success or failure of angioplasty treatments. In addition, the success rate may also depend on the stenosis type. Hence, for a particular stenotic artery, the optimal intervention can only be identified by studying the influence of factors such as stent type, strut thickness, geometry of the stent cell, and stent-artery radial mismatch with the wall. We propose a methodology that allows a set of stent parameters to be varied, with the aim of evaluating the difference in the mechanical environment within the wall before and after angioplasty with stenting. Novel scalar quantities attempt to characterize the wall changes in form of the contact pressure caused by the stent struts, and the stresses within the individual components of the wall caused by the stent. These quantities are derived numerically and serve as indicators, which allow the determination of the correct size and type of the stent for each individual stenosis. In addition, the luminal change due to angioplasty may be computed as well. The methodology is demonstrated by using a full three-dimensional geometrical model of a postmortem specimen of a human iliac artery with a stenosis using imaging data. To describe the material behavior of the artery, we considered mechanical data of eight different vascular tissues, which formed the stenosis. The constitutive models for the tissue components capture the typical anisotropic, nonlinear and dissipative characteristics under supra-physiological loading conditions. Three-dimensional stent models were parameterized in such a way as to enable new designs to be generated simply with regard to variations in their geometric structure. For the three-dimensional stent-artery interaction we use a contact algorithm based on smooth contact surfaces of at least C^1 -continuity, which prevents numerical problems known from standard facet-based contact algorithm. The proposed methodology has the potential to provide a scientific basis for optimizing treatment procedures and stent geometries and materials, to help stent designers examine new stent designs ‘virtually’, and to assist clinicians in choosing the most suitable stent for a particular stenosis.

¹Corresponding author.

1 Introduction

Balloon angioplasty is a well-established interventional procedure which aims at reducing the severity of atherosclerotic stenoses. Unfortunately, although most of the treatments are performed with stenting nowadays, the procedure still can fail due to resistance to dilation, thrombosis and stress-induced tissue growth such as neointimal hyperplasia. The latter biological process is triggered by inflammation, granulation and cellular proliferation which is as a consequence of the changed stress situation in the arterial wall. Nevertheless, balloon angioplasty with stenting improves the short-term success rate and reduces rates of restenosis in long term [1], [2], and, consequently, the need for further interventions when compared to standard angioplasty procedures. The Restenosis Stent (REST) Study [3], for example, compared coronary-artery stenting with balloon angioplasty for restenotic lesions after initial balloon angioplasty. The randomized study considered a total of 383 patients with restenosis after balloon angioplasty who were randomly assigned to Palmaz-Schatz stent placement or repeat (standard) balloon angioplasty. Angiographic restenosis ($> 50\%$ follow-up diameter stenosis) at six months was lower in stent-treated patients (18% versus 32% in balloon angioplasty-treated patients; $p = 0.03$). Several other randomized trials confirmed a better clinical outcome of stent placement over balloon coronary angioplasty alone (see, for example, [4]).

An angioplasty intervention at which an endovascular stent is inserted into the artery differs significantly from a standard angioplasty procedure: (i) the struts of the stent impose focal vascular trauma [5], (ii) or an early thrombus (generated within days) may serve as a scaffold for subsequent cell proliferation and intimal hyperplasia ([1], [2], [6]). Thereby, platelet-rich mural thrombi form over the stent struts, into which inflammatory cells migrate from the circulation and the adventitial vasa vasorum. In addition, (iii) permanent (non-physiologic) rather than transient stresses and strains are generated around the stent when it expands, which may lead to cellular proliferation ([7], [8]), and (iv) a foreign material remains in the injured artery [9]. The influence of a foreign material on the vasculature was clearly demonstrated with stents that were intended to be gradually resorbed. In particular, it was shown that the use of a PET polymer stent can produce intense proliferative neointimal response that may result in complete vessel occlusion within 4 to 6 weeks [10].

Several clinical studies related to stenting were attributed to device-dependent factors such as the stent design ([11], [12], [13], [14]) or the deployment technique ([15], [12]). Other clinical studies are concerned with vascular remodeling. The work [16], for example, has shown that vascular remodeling after angioplasty is regulated by wall shear stresses and stresses within the wall. In addition, elevated wall shear stresses after successful angioplasty were identified as predictive quantities for target lesion revascularization and associated restenosis ([17], [18], among others). In recent years a number of approaches aim to reduce or prevent restenosis; most notably is the use of drug-eluting stents, which demonstrate a remarkable efficacy and safety in preventing neointima formation and recurrent restenosis ([19], [20]). Intravascular brachytherapy is effective to reduce in-stent restenosis, however, the recurrence after brachytherapy is still significant [21], [22]. It is important to note that the mechanical injury to the vessels is not eliminated with these recently developed procedures so that the present study appears still meaningful in order to identify the biomechanical nature of the stenting procedure.

Our approach intends to predict the outcome of patient-specific angioplasty treatment on a computational basis. The proposed approach allows insights into the development of mechanical stresses during inflation, leading to ‘controlled vessel injury’ [23], and provide computational assessment of parametric stent designs. Stress-induced tissue growth and undesirable arterial injury such as intramural hemorrhage may probably be avoided by selecting the most suitable angioplasty treatment and stent for an individual stenosis. The angioplasty treatment can be performed with several parameters, which can be varied on a computational basis to get the change of the mechanical environment during dilation, and to find the optimal treatment for a particular stenosis type. As a starting point we alter

- (i) the type of stent cells, which is chosen similar to three commercial products,
- (ii) the geometry of stent cells and stent struts,
- (iii) the radial mismatch between the smallest lumen diameter in the stenosis and the expanded stent diameter (nominal stent diameter),

and analyze the relationship between these parameters. They were shown to be crucial for decreasing the risk of in-stent restenosis after stent placement (which, in virtually all cases, is

neointimal proliferation [24]), and, consequently, to obtain a successful clinical outcome of the stenting process (see, for example, [25], [26], [27]). It is straightforward, however, to include other treatment parameters in the proposed methodology.

The determination of an optimal treatment, however, requires a quantification of the changes (here only mechanical) in the arterial wall during inflation and stent deployment. We propose the following strategy: first, evaluate mechanical field quantities, which are based on nonlinear finite element analyses; second, evaluate indicators with the goal to replace the field quantities by scalars enabling the establishment of a ‘ranking’ among the results. These indicators are derived numerically and allow a characterization of

- (i) the change of the intimal pressure caused by the struts of the stent,
- (ii) the stress change within the arterial wall caused by the stent, and
- (iii) the luminal change due to angioplasty.

Hence, as known, vascular interventions that maximize just the lumen diameter provoke extensive intimal hyperplasia due to local damage of the vascular wall [11]. Hence, choosing the most suitable stent and treatment procedure for a certain stenosis is always a tradeoff between lumen gain and locally induced arterial injury, which is postulated to be responsible for the development of smooth muscle cell proliferation, neointimal hyperplasia and refractory restenosis, see the review [28]. The idea is now to, somehow, minimize the changes of the intimal pressure and the arterial wall stresses by maximizing the lumen diameter increase for a particular stenosis. We will demonstrate which influence certain treatment parameters have on the introduced indicators.

Since our approach attempts to find an optimal solution on a patient-specific basis, a reliable numerical model considering as much information as possible is a prerequisite. The proposed methodology combines numerical models for the artery and the stent, and allows the investigation of the interaction of the stent with the vascular wall. The design of the arterial model is based on our recent works [29], [30]. In the present study we investigate one individual human stenosis. The geometric model of the considered stenosis was composed of eight different tissue components, which were specified from **high resolution Magnetic-Resonance**

Images (hrMRI) and reconstructed by means of **Non-Uniform Rational B-Splines** (NURBS). Generation of three-dimensional finite element meshes serves as the basis for numerical analyses, and possible mesh refinement allows an error estimation of the numerical solutions. Data from mechanical tests are used to establish constitutive models and associated parameters for the individual components. Since the material properties of arterial components *in vivo* are not available and the resolution of *in vivo* hrMRI is still insufficient yet, our approach is performed in an *in vitro* setting. However, the proposed methodology may be applied to an *in vivo* situation when hrMRI improves and the material properties may be estimated appropriately (for example, through inverse finite element modeling). We use then numerical models for three different stents, whereby the geometric structure of the stents are parameterized to allow convenient parameter studies, and the development of new stent design. A novel contact algorithm, recently documented in [31], is aimed at simulating the interaction between the artery and the stent, and overcomes stability problems which were shown to arise in typical simulations of angioplasty [32]. Well known stability problems are caused by non-smooth (C^0 -continuous) interacting bodies. To avoid these problems, the contact algorithm employs subdivision surfaces to obtain smooth contact surfaces of at least C^1 -continuity everywhere. Many works investigate the mechanics of arterial walls and stents separately, however, very few studies treat the interaction as a computational contact problem (see [33], [29], [30] and [34], [35]). To the authors' knowledge the present approach is the first which allows to (i) analyze the three-dimensional interaction between stent models and patient-specific wall models by considering image data and mechanical tests performed at body temperature, (ii) quantify the change in the mechanical environment which occurs during stent placement, (iii) compare the effects of different parameters to identify optimal stent designs. Based on this approach stents may be parameterized such that novel designs (for example, geometry, material composition) and placement protocols (for example, balloon selection, inflation pressure, delivery and deployment system) are to be developed in order to minimize vascular injury and to optimize long-term success. The methodology may eventually assist clinicians in choosing a particular stent with the goal to improve the clinical outcome.

2 Methods

We start by defining scalar indicators to characterize the outcome of angioplasty with stenting, and proceed by providing (numerical) models for the arterial wall and the stent. Finally, the stent-artery interaction with related boundary conditions and the process of loading is described.

2.1 Indicators to characterize the outcome of angioplasty with stenting

Although our numerical model can not yet simulate microscopic effects such as vascular injury or cell proliferation, (high) stress concentrations can be predicted and interpreted as a very likely source for vascular injury and remodeling (see e.g. [36]).

In a previous paper [30] we analyzed the local stress distribution within the specimen during angioplasty. In the present work we use the gained knowledge for the definition of indicators, which may allow to quantify the change in the mechanical environment and the luminal change during angioplasty with a stent. These indicators are scalar quantities which should allow a judgement upon the advantages and disadvantages of taking one stent product or another. In this section we define three different scalar indicators to characterize (i) the intimal pressure concentration caused by the stent struts, (ii) the stress change within the arterial wall, and (iii) the luminal change during stenting.

2.1.1 Intimal pressure concentration caused by the stent struts

The pressure, which occurs between the contact area of the stent struts and the intimal surface of the arterial wall is in part one determinant for restenosis. Stent struts may cause focal deep vascular trauma [5], [11], and endothelial cell denudation [35]. The elevated pressure around the stent struts may lead to intimal laceration and direct injury to medial smooth muscle cells, which was shown to be related to neointimal hyperplasia (see, e.g., [12]).

We propose that the (normalized) change of the intimal pressure caused by the struts of the stent, denoted by D_1 , is expressed as

$$D_1 = \sum_{j=1}^{n_b} \frac{\Delta p_j}{p_{\text{MAP}}} \kappa_j, \quad \text{with} \quad \Delta p_j = p_{j,\text{post}} - p_{\text{MAP}}, \quad (1)$$

where j indicates the element number on the intimal surface, and n_b is the total number of elements forming the intimal surface. The factor κ_j is a measure for the surface of element j covered by the stent struts, while the value $p_{j,\text{post}}$ is the contact pressure on the surface of element j after stenting ($(\bullet)_{\text{post}}$) due to the stent struts and the mean arterial pressure. A detailed computation of $p_{j,\text{post}}$ and κ_j is illustrated in the Appendix. The mean arterial pressure before angioplasty is denoted by p_{MAP} . For the numerical simulation we have used $p_{\text{MAP}} = 13.3$ (kPa). The pressure difference on the surface of element j after and before angioplasty is then given by Δp_j .

Note that the study in [37] evaluates the deflection of the tissue between the struts of different stent products (called ‘prolapse’ or ‘draping’). In clinical studies this lumen loss due to deflection of the tissue was associated with the appearance of restenosis (see, for example, [38]). Since prolapse depends on the contact pressure and the spacing between the stent struts, the contact pressure may be used as an indicator instead of the deflection of the tissue between the struts. This alternative indicator has the special merit that it directly depends on the important measure of the strut width, which is hardly the case for the prolapse indicator.

2.1.2 Stress change within the arterial wall caused by the stent

To study the development of stresses within the arterial wall during angioplasty, we compute the Cauchy stress differences which occur in the finite elements. In particular, for an element with number i , the stress difference $\Delta\sigma_i$ is according to

$$\Delta\sigma_i = (\sigma_{\text{post}} - \sigma_{\text{pre}})_i, \quad (2)$$

where $(\sigma_{\text{post}})_i$ and $(\sigma_{\text{pre}})_i$ denote the circumferential Cauchy stresses for element i after and before angioplasty, respectively. Note that $(\sigma_{\text{pre}})_i$ is the Cauchy stress in element i during the mean arterial pressure of 13.3 (kPa). Although, in principle, any other stress components could be used, our recent study [30] has shown that the circumferential stresses are the one most altered during angioplasty.

Subsequently, we are just interested in the Cauchy stress differences in a certain tissue component l during angioplasty, which reach a (given) certain limit. Hence, we define this limit by $\Delta\bar{\sigma}_l$ for a stress *increase*, and by $\Delta\underline{\sigma}_l$ for a stress *decrease*. The stress difference is then

weighted by the volume Ω_i of the element i , in which it occurs. Hence, we define the merit functions χ_i^1 and χ_i^2 for a stress increase and a stress decrease in a particular element i , respectively, and write

$$\chi_i^1 = \begin{cases} \Delta\sigma_i\Omega_i & \text{if } \Delta\sigma_i > \Delta\bar{\sigma}_l \\ 0 & \text{otherwise} \end{cases} \quad \chi_i^2 = \begin{cases} |\Delta\sigma_i|\Omega_i & \text{if } \Delta\sigma_i < \Delta\underline{\sigma}_l \\ 0 & \text{otherwise} \end{cases} \quad (3)$$

with $1 \leq l \leq N$, where N is the total number of tissue components. For example, eq. (3)₁ means that the stress change in a particular element i located in the tissue component l is only considered if the stress σ_{post} in that element after angioplasty is about $\Delta\bar{\sigma}_l$ higher than the stress σ_{pre} before angioplasty.

The stress change within the arterial wall caused by the stent may then be defined by the (most general) measure

$$D_2 = \frac{\sum_{i=1}^n (w_1\chi_i^1 + w_2\chi_i^2)}{\sum_{i=1}^n (\sigma_{\text{pre}})_i\Omega_i}, \quad (4)$$

where $w_1, w_2 \in [0, 1]$ are weighting functions with the condition $w_1 + w_2 = 1$, and n denotes the total number of finite elements. If $w_1 = w_2$, this means that a stress increase is equally weighted as a stress decrease.

An alternative version of (4) is obtained by assuming that the values $\Delta\bar{\sigma}$ and $\Delta\underline{\sigma}$ are the same for all tissue components. In particular, for the numerical studies performed in the next section, we have assumed that only stress increases are considered ($w_2 = 0$), and that any stress increase, which might occur during angioplasty is taken into account ($\Delta\bar{\sigma}_l = 0$). This leads to the simplified version of (4), already employed in [30], which is

$$D_2 = \frac{\sum_{i=1}^n \Delta\sigma_i\Omega_i}{\sum_{i=1}^n (\sigma_{\text{pre}})_i\Omega_i}, \quad (5)$$

where $\Delta\sigma_i$ is defined in (2).

2.1.3 Luminal change during stenting

For the luminal change due to angioplasty, it is only meaningful to consider the smallest luminal area. Hence, we define a factor LG expressing the **Luminal Gain**, i.e.

$$LG = \frac{\Delta A}{A_{\text{pre}}}, \quad \text{with} \quad \Delta A = A_{\text{post}} - A_{\text{pre}}, \quad (6)$$

where A_{pre} is the smallest inner cross-section of the artery before angioplasty and stenting, and A_{post} is the cross-section at the same location as A_{pre} after angioplasty and stenting. Consequently, ΔA is the area difference and a meaningful measure for the area change during the treatment.

2.2 Arterial model

This section provides information for the design of a model for one specific diseased iliac artery, as documented in [39]. Here we describe how the three-dimensional arterial geometry was reconstructed by means of magnetic resonance images and NURBS curves. The performed mechanical tests to identify the anisotropic quasi-static stress-stretch responses of the different tissue types are briefly described, and appropriate constitutive models provided. Finally, the spatial discretization of the individual tissues with capable finite elements serve then the basis for the arterial model.

2.2.1 Material

An external iliac artery (female, 65.0 year old) was harvested during autopsy within 24 hours from death (detailed information about the related anamnesis is provided in Table 1 of [39], i.e. specimen I therein). The investigated artery has an atherosclerotic lesion of type V, according to Stary et al. [40], which contains mainly reparative smooth muscle cells and fibrous tissue and additionally two or more lipid pools of unequal size separated from each other by cells and fibrous tissue. Two cross-sectional macroscopic views of the stenotic iliac artery are provided in Fig. 1, Sections A-A and C-C. The axial *in situ* pre-stretch, defined as the ratio of *in situ* length to *ex situ* length, was calculated to be 1.052. Use of autopsy material from human subjects was approved by the Ethics Committee, Medical University Graz, Austria.

In order to detect the three-dimensional geometry for reconstruction purposes, we use hrMRI. The detailed procedure and the associated histological analyses required to identify the underlying tissue type are provided in [39]. For this lesion eight different tissue types were considered: the non-diseased intima I-nos¹, fibrous cap I-fc (fibrotic part at the luminal border), fibrotic intima at the medial border I-fm, calcification I-c, lipid pool I-lp, non-diseased media M-nos, diseased fibrotic media M-f and adventitia A [29, 30, 39]. This classification has resulted in a separation of the diseased vessel wall (compare with Fig. 1) that is (solid) mechanically representative and that covers the gross histological composition of the stenosis (see, for example, Stary et al. [40]). This separation is also physically feasible using surgical instruments.

2.2.2 Geometric model

For each scanned image-based cross-section the borders of the arterial components were traced automatically by a set of points. These points were then fitted by NURBS curves using a least-square fitting procedure. Finally, the curves were combined along the arterial axis in order to get the boundary surfaces of the different tissue components. NURBS representations have the advantage that they enable discretizations of different mesh densities to be based on a single smooth surfaces. They provide a suitable basis for mesh adaption procedures that allow mesh refinement with respect to the (original) reference geometry, and for error estimation.

The geometry of the harvested stenotic iliac artery is shown in Fig. 1. In order to display the path of the lumen over the whole length of the specimen, which is tortuous, the cutting plane for Section D-D was chosen to be out of the center (for the location of D-D compare with the other sections).

2.2.3 Mechanical testing and physical modeling

Mechanical tests were performed on a computer-controlled, screw-driven high-precision tensile testing machine by integrating. For the determination of the passive, quasi-static stress-stretch response of the individual tissue components, rectangular stripe samples with axial and circumferential orientations were excised from the specimen and immersed in a calcium-free physi-

¹The abbreviation ‘nos’ is frequently used in histopathology and stands for **n**ot **o**therwise **s**pecified. In the context of the present study it means ‘no appreciable disease’, or, more precisely ‘non-atherosclerotic’.

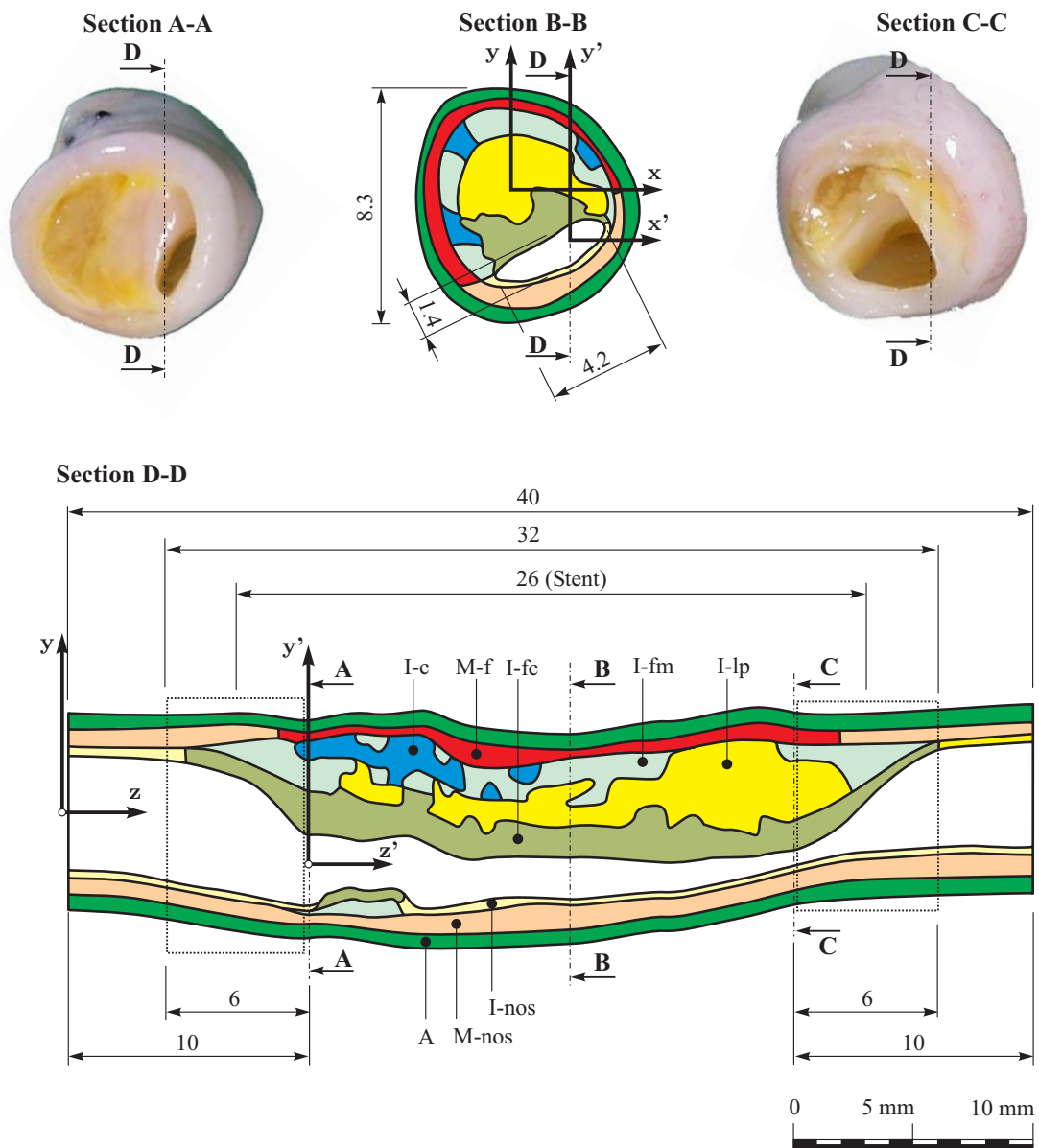


Figure 1: Sections of the analyzed external iliac artery. Section B-B is the region with the smallest lumen diameter of 1.4 (mm). The tissue components are: adventitia (A), non-diseased media (M-nos), non-diseased intima (I-nos), fibrous cap (I-fc), lipid pool (I-lp), calcification (I-c), fibrotic intima at the medial border (I-fm) and diseased media (M-f). The regions for the analysis of edge effects, as described in Sec. 3.2.2, are denoted by the areas with dotted frames (Section D-D).

ological 0.9% NaCl solution at $37^\circ\text{C} \pm 0.1^\circ\text{C}$. The lipid pool I-lp was not tested because of its ‘butter-like’ consistence. For the artery investigated in this paper the size of the tissue components I-nos and I-fm was not big enough to prepare appropriate stripe samples for testing. A description of the mechanical tests, and the obtained stress-stretch responses for 7 different tissue types stemming from 9 human high-grade stenotic iliac arteries are documented in [39]. Thereby, all tissue samples were stretched far beyond the physiological loading domain up to failure so that the range of deformations induced by the stent is captured.

In order to model the material response each component of the stenotic artery is assumed to behave as an (nearly) incompressible composite reinforced by two families of collagen fibres. The (three-dimensional) statistical distribution of fibre directions are characterized by two symmetrically arranged families of collagenous fibres whose mean directions are represented by the unit vectors \mathbf{M} and \mathbf{M}' , and it is these directions that render the material properties anisotropic.

According to [41] we consider a strain-energy function relative to the reference configuration in the decoupled form

$$\Psi = U(J) + \bar{\Psi}(\bar{I}_1, \bar{I}_4, \bar{I}_6), \quad (7)$$

where the function U is a purely volumetric contribution and $\bar{\Psi}$ is a purely isochoric contribution to the strain energy Ψ . In (7) $J = (\det \mathbf{C})^{1/2}$ is the local volume ratio, while $\mathbf{C} = \mathbf{F}^T \mathbf{F}$ denotes the right Cauchy-Green tensor and \mathbf{F} is the deformation gradient. In addition, $\bar{I}_1 = \text{tr } \bar{\mathbf{C}}$ is the first invariant of the modified right Cauchy-Green tensor $\bar{\mathbf{C}} = J^{-2/3} \mathbf{C}$, and $\bar{I}_4 = \bar{\mathbf{C}} : \mathbf{M} \otimes \mathbf{M}$, $\bar{I}_6 = \bar{\mathbf{C}} : \mathbf{M}' \otimes \mathbf{M}'$. We take the strictly convex function $U = \kappa(J - 1)^2/2$, which is motivated mathematically. Therein, the bulk modulus κ serves as a user-specified (positive) penalty parameter, which is independent of the deformation and chosen through numerical experiments. Clearly, with increasing κ the violation of the constraint is reduced. If we take the restriction on the value $\kappa \rightarrow \infty$, the constraint condition is exactly enforced, and then eq. (7) represents a functional for an incompressible material with $J = 1$.

For the function $\bar{\Psi}$ we use the particularization

$$\bar{\Psi}(\bar{I}_1, \bar{I}_4, \bar{I}_6) = \mu(\bar{I}_1 - 3) + \frac{k_1}{2k_2} \sum_{\alpha=4,6} \left\{ \exp\{k_2[(1 - \rho)(\bar{I}_1 - 3)^2 + \rho(\bar{I}_\alpha - 1)^2] - 1\} \right\}, \quad (8)$$

where $\mu > 0$ and $k_1 > 0$ are material parameters with the dimension of stress, and $k_2 > 0$, $\rho \in [0, 1]$ are dimensionless material parameters. The function $\bar{\Psi}$ is sufficiently general to

capture the basic anisotropic features of tissue responses of human atherosclerotic plaques, as observed in the experiments [39]. Note that for the limit $\rho = 1$ we get the constitutive equation, as proposed in [41] and successfully used to model healthy human arteries, while for the limit $\rho = 0$ we get an (isotropic) constitutive equation, as documented in [42]. In addition, we assume that the anisotropic term in (8) contributes when either $\bar{I}_4 > 1$ or $\bar{I}_6 > 1$ or both. For example, if $\bar{I}_4 \leq 1$ and $\bar{I}_6 > 1$, then only \bar{I}_6 contributes to $\bar{\Psi}$.

In the following we use the same form of strain-energy function (8) for each tissue component but with a different set of material constants and different direction vectors \mathbf{M} and \mathbf{M}' associated with the structure. We specify the components of the direction vectors for each tissue component using a cylindrical polar coordinate system and neglect the components of the (collagenous) fibre orientations in the radial direction. Hence, instead of \mathbf{M} and \mathbf{M}' we use the angle φ ($^\circ$), which occurs between the fibres (arranged in symmetrical helices) and the circumferential direction in the specific tissue component [41]. However, since we do not have particular information about the fiber orientations within the tissue components, the angle φ is treated here as a phenomenological parameter. Consequently, particular material parameters of the arterial components were obtained by fitting the constitutive model to corresponding anisotropic data provided in [39]. The Levenberg-Marquardt algorithm has been used for the least-square fit. The according best-fit parameters and the associated error measures are summarized in Table 1. Since no experimental data were available for the tissue components I-nos and I-fm, we have adopted the mean parameter values from various investigated iliac arteries according to [43]. As a measure for the ‘goodness of fit’ linear correlation coefficients, $r(S_{\theta\theta})$, $r(S_{zz})$ say, were calculated for the second Piola-Kirchhoff stresses in both the circumferential and axial directions of the stripe to be considered. In addition, a second ‘error measure’, ϵ say, is introduced, which is the root mean square error (per statistical degree of freedom) normalized in regard to a reference stress. For a detailed description of these measures the reader is referred to [44]. According to [39] the average Young’s modulus for the calcification I-c, which, interestingly, has shown linear behavior, is 12.6 (MPa). Assuming nearly incompressible response we have used the value $\mu = 2.25$ (MPa) for I-c. The value for the lipid pool I-lp was taken from [30] to be $\mu = 0.05$ (kPa).

With arguments entirely similar to those in [30] we model the non-diseased intima I-nos

and the non-diseased media M-nos by a constitutive equation capturing nonrecoverable deformations [45]. The inelastic response is described with an initial yield stress τ_0 and a linear hardening parameter h , see Table 1. The ratios of the (penalty) parameters κ to the moduli μ for the arterial components were chosen to be roughly equivalent to two to three orders of magnitude.

2.2.4 Finite element discretization

Based on the NURBS geometry, as described in Section 2.2.2, meshes of varying density can be generated. For the investigated arterial specimen we created three discretizations with different mesh densities. This allowed a comparison of the numerical solutions and an assessment if the mesh density is sufficient for the desired accuracy. The meshes consist of 945, 3150 and 9765 3D-elements.

In general, we used eight-node isoparametric hexahedral elements. Only for the elements adjacent to the master contact-surface we used 20-node elements, which form an interface between the smooth contact surface description and the finite element discretization [31]. Both element types use linear interpolation functions for the displacement field and (the same) discontinuous (constant) functions for the remaining field variables (dilatation and pressure), leading to the $Q1/P0$ -element. The volumetric variables are eliminated on the element level. This well-known technique circumvents numerical difficulties which arise from the overstiffening of the system associated with the analysis of *isochoric* constitutive responses of the arterial wall. For a detailed derivation see, for example, [46].

2.3 Stent model

2.3.1 Geometry and structure

Parametric design is a useful technique in engineering practice when products are tailored to fit specific customer needs or when numerical optimization is used to generate the ‘optimal’ design of a product. Both requirements are to be addressed for the design of novel stents regarding their geometric structure. Basically, the parameterization of a stent involves the *geometry of the stent cells*, the *geometry of the stent struts*, which may vary across the stent length, and the *nominal*

stent diameter and the *length*. Local changes in the geometries of the stent cells and struts are useful, for example, to specify different stiffnesses at the ends of a stent in order to avoid edge effects (see Section 3.2.2).

In this study we investigate three different types of stent cells, which are based on products that are (or were) available commercially. In particular, for our study we employ shapes of stent cells used in products such as (a) the Multi-Link-TetraTM stent (Guidant), (b) the NIROYALTM Elite stent (Boston-Scientific) and (c) the InFlowTM-Gold-Flex stent (InFlow Dynamics). For subsequent use we will refer to these stent types as S1, S2 and S3, respectively. The geometries of the stent cells were traced from photographs.

Software for appropriate parameterization of stent cells. Here we propose an efficient strategy of stent parameterization. We developed a software, which is able to parameterize (i) the geometry of the stent cells, (ii) the geometry of the struts (with width s_w , measured in the circumferential direction, and with thickness s_t , measured in the radial direction), and (iii) the overall dimensions of the stent (i.e. nominal diameter D , number of cells in the axial direction m and in the circumferential direction n ; D refers to the stent diameter achieved at any axial position, while the balloon is fully inflated). For the parameterization of the stent cell the software requires information about: (i) the cell type (S1, S2, S3), (ii) the geometrical quantities to be parameterized (see the upper panels of Fig. 2; each dimension, denoted by lower case letters, represents a parameter), and (iii) a set of rules describing how the parameters depend on each other. As input data we have only used the two dimensions b and d , while all others dimensions are based upon these two. The lower panels of Fig. 2 show the generated 3D views of the different stents. The software also allows to generate a finite element mesh for the individual parameterized stent.

Consequently, the indicators, as defined in Section 2.1, enable the study of the ability and performance of a particular stent design (given by the parameters discussed) for a particular stenotic artery to be treated.

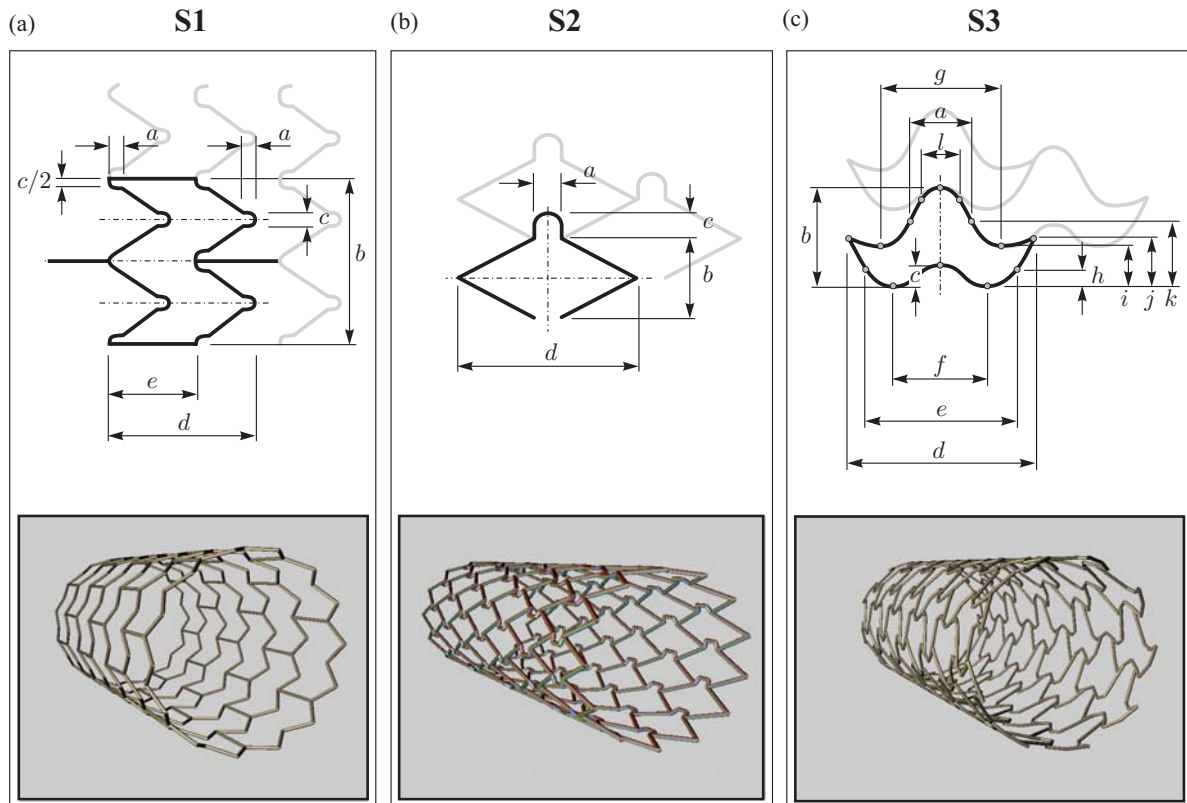


Figure 2: Three different stent geometries described by a number of (geometrical) parameters, denoted by lower case letters (upper panels). The cell types are based on products that are (or were) available commercially: (a) Multi-Link Tetra™ stent (Guidant): S1, (b) NIROYAL™-Elite stent (Boston-Scientific): S2, (c) InFlow-Gold-Flex™ stent (InFlow Dynamics): S3. The lower panels show the generated 3D views of the different stents.

2.3.2 Material modeling

Since stent manufacturers do not provide details about the alloys used for their stent products, as a first approach, we have adopted the material properties for stainless steel for all three stents. The parameters to be chosen are $E = 2.0 \cdot 10^5$ (N/mm²) and $\nu = 0.3$. The plastic behavior of the stent is described by a yield stress of $\sigma_y = 2.1 \cdot 10^3$ (N/mm²). For the finite element formulation we have used a neo-Hookean model for the elastic regime and a J_2 -model for the plastic regime [47] (no hardening was considered).

2.3.3 Finite element discretization

For the discretization of the stents we have used hexahedral finite elements with quadratic shape functions. The meshes for the stents were generated automatically by the software. The parameters defining the different stent cells are summarized in Table 2. For each stent two input parameters (b and d) are specified, which are indicated in the table by the symbol \bullet .

The strut width and the strut thickness were assumed to be $s_w = 140$ (μm) and $s_t = 450$ (μm), respectively. For each of the stent types we have assumed four different nominal stent diameters D . We have assumed that the ratio of the actual metal surface in contact and the arterial wall surface, i.e. the metal-to-artery ratio R_{ma} , is constant with 0.15, with $R_{\text{ma}} = ks_w n / (D\pi - ks_w n)$, where k denotes the number of struts for one stent cell in the circumferential direction ($k = 5$ for S1, and $k = 2$ for S2 and S3). The number of cells m in the axial direction is 7 for all stent types, which gives a stent length of about 26.0 (mm). The number of cells n in the circumferential direction was computed from the given metal-to-artery ratio, and the parameter b is given to be $D\pi/n$. Specific parameters for the three cell types are summarized in Table 3.

2.4 Finite element simulation

The simulations were carried out on a parallel cluster consisting of 24 nodes and one master connected with an internal 300GB RAID-System together with an external 1TB fileserver. The performance of the system is about 14Gflops and allows high performance computing necessary to solve this type of nonlinear boundary-value problems. The assembly of the stiffness matrices and the solution process of the linear systems of equations were computed in parallel. Since the systems of equations are sparse and not symmetric (due to plasticity and pressure boundary loadings), they were solved using a Krylov-subspace method. In particular, we used a stabilized version of an iterative bi-conjugate gradient solver [48]. The systems were preconditioned by successive overrelaxation.

Next we briefly describe the employed contact algorithm, the applied boundary conditions and the loading procedure.

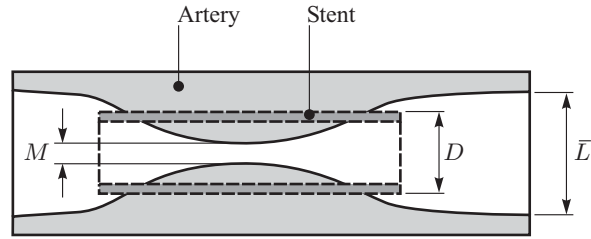


Figure 3: Mismatch $\Delta M = D - M$ between the smallest lumen diameter M in the stenosis and the diameter D of the expanded stent. The lumen diameter of the healthy arterial region is characterized by \bar{L} .

2.4.1 Stent-artery interaction

As a rule of thumb, in clinical practice, the nominal diameter D of an expanded stent should be similar to the lumen diameter of the related healthy arterial region, \bar{L} say — in our case 6.0 (mm). Therefore, during stent expansion, there appears to be a radial mismatch $\Delta M = D - M$ between the smallest lumen diameter M in the stenosis (in our case $M = 1.4$ (mm)) and the expanded nominal stent diameter D . For an illustration of the geometrical situation see Fig. 3. Hence, according to Table 3, from the diameters D we get four different values of the mismatch ΔM , namely for 1.6, 2.6, 3.6, 4.6 (in millimeter). Consequently, a value of $\Delta M = 4.6$ (mm) reestablishes the original lumen of $\bar{L} = 6.0$ (mm), provided that no recoil occurs. Note that the stent may also be potentially subject to migration depending on the radial mismatch.

Typically, during a balloon-angioplasty procedure the pressure load is applied to a balloon expanding a stent. According to [32] this approach may render the discretized system unstable. Hence, in order to avoid additional complexity, we ignored the balloon and applied the (deformation dependent) pressure load directly on the stent struts, as, for example, performed in [49], [32]. In contrast to prescribed displacements on the stent struts, as used, for example, in [30], the application of pressure loads on the stent struts has the big advantage that, for example, the important ‘dog-boning’ effect of stents can be simulated. For a discussion of the relationship between stent geometries and dog-boning effects [33]. Note, however, that this (simplified) approach could have some influence on the numerical results, because the balloon would likely bulge out between the struts during stent expansion, and would, consequently, expand the ar-

terial wall to a larger extent than the portion of the wall in contact with the struts. To capture these phenomena numerically is a rather costly task.

For the interaction between the stent and the arterial wall we have used a contact algorithm, which uses subdivision surfaces for the interpolation [31]. Note that a standard facet-based contact algorithm (with C^0 -continuity of the contact surface at the element edges) may lead to typical numerical problems during a simulation such as oscillation of contact forces, non-realistic pressure jumps, contact cycling and loss of quadratic convergence of the nonlinear solution scheme. Although our contact approach is able to capture frictional behavior, we carried out the simulations without friction since reliable coefficients describing the frictional behavior between the intimal surface and the stent are not available yet.

2.4.2 Application of boundary conditions

The geometry of the artery is embedded in the x, y, z -coordinate system. Since the artery has an eccentric stenosis it is not straightforward to describe appropriate boundary conditions for the stent expansion. Hence, we introduce an additional x', y', z' -coordinate system, which is the reference system for the stent expansion. The z' -axis does not intersect with the arterial tissues (see Fig. 1).

Artery. In order to avoid rigid-body motions we have to fix a total of six degrees of freedom of three nodes. By only fixing three nodes of the artery we would end up with an ill-conditioned system of equations, which could hardly be solved. Because of that we have fixed all z -displacements on both end faces of the artery. In addition, we fixed all x -displacements and y -displacements for the nodes of the adventitia, which are located at the vicinity of the y', z' -plane and the x', y' -plane, respectively. For the computation of the indicators described in Section 2.1 we have ignored the contributions, which arise from the finite elements adjacent to both end faces of the artery. These contributions would not be meaningful because of the chosen boundary conditions.

Stent. In order to avoid rigid-body motions for the stent the z' -displacements are fixed for all nodes on one end of the stent. In addition, the x and y -displacements are fixed for all nodes located in the y', z' -plane and the x', z' -plane, respectively (see Fig. 1).

Note that in a clinical situation both the artery and the stent will deform during the insertion process for this type of tortuous lumen investigated. However, the numerical simulation of this process is associated with high computational cost, which we wanted to avoid. Therefore, a strategy is chosen by which the undeformed stent is placed with overlap in the tortuous lumen. Then, in a few load steps, the penalty parameter, which enforces the contact constraint, is gradually increased from zero to a desired value of about 10^6 . This strategy aligns the stent with the arterial inner surface in a numerically efficient way. Now, due to the applied boundary conditions, the artery and the stent are constrained such that there is no relative motion normal to the x', z' and y', z' -planes.

2.4.3 Loading procedure

In order to simulate the physiological loading situation two loads are applied on the artery: (i) mean arterial pressure of 100.0 (mmHg) (i.e. 13.3 (kPa)) on the entire inner surface of the artery by (displacement dependent) surface loads, (ii) axial pre-stretch of 1.052 for all nodes located on one end face of the artery by displacement boundary conditions (all nodes on the other end face have fixed z -displacements). After applying these physiological loads the displacement boundary conditions on one end face of the artery are replaced by equivalent reaction forces. This replacement leads to physically more realistic simulation during subsequent loading.

To expand the stent-artery system, we apply displacement dependent surface loads on the inner side of the stent struts. After full expansion, the pressure loads on the struts are removed gradually. Throughout this loading process, the blood pressure of 100.0 (mmHg) on the inner wall of the artery remains.

3 Results

We study the effect of different stent geometries S1, S2, S3, as discussed in Section 2.3, on the stenotic iliac artery described in Section 2.2.

As a representative example, Fig. 4 shows the numerical results in form of circumferential Cauchy stress distributions. The cutting planes indicate stresses before (see Fig. 4(a)) and after stenting (see Fig. 4(b)) at locations, where changes in stress due to stenting are most pro-

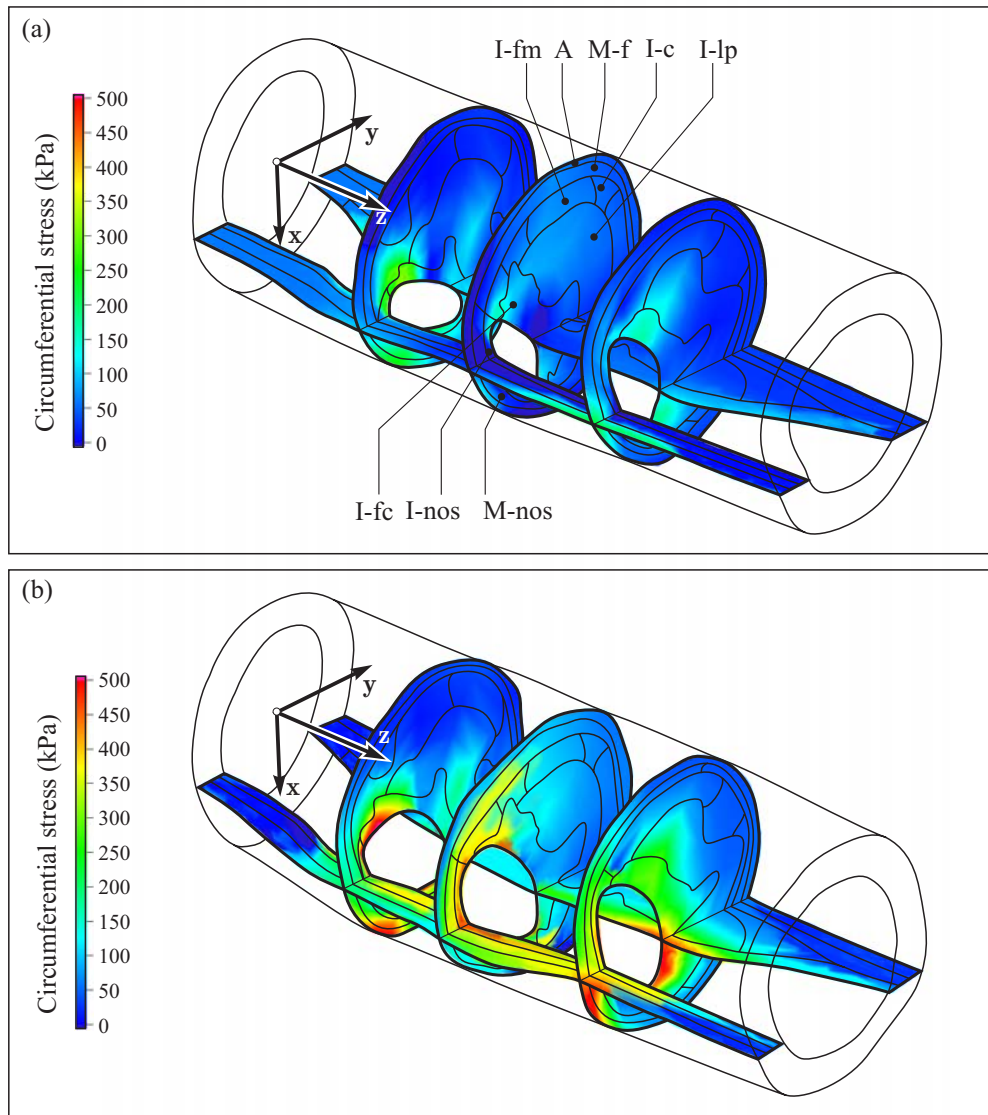


Figure 4: Circumferential Cauchy stress distributions in the arterial wall before (a), and after stenting for stent S1 at $\Delta M = 3.6$ (b). The only load applied in both configurations is the mean arterial pressure of 100.0 (mmHg). Stresses are projected onto cutting planes at $x = 2.0$ (mm), and $z = 12.0$ (mm), $z = 20.0$ (mm), $z = 18.0$ (mm). The cutting planes were selected at locations, where changes in stress due to stenting are most pronounced.

nounced. For the image shown in Fig. 4(b) the stent S1 was used with $\Delta M = 3.6$. As can be seen, stenting induces large stress concentrations in the non-diseased area, while the diseased area remains mainly unchanged. Within the diseased part, the fibrous cap (I-fc) becomes remarkably stressed. High stress in this plaque component may lead to tissue failure and to an increased risk of thrombus formation [30].

In the following we characterize the mechanical effect after deployment and expansion of the stent up to the diameter D by the indicators D_1 , D_2 and LG , as described in Sec. 2.1. The study is based on a variation of (i) the strut thicknesses for the entire stent, (ii) the strut thicknesses for the end cells of the stent only, and (iii) of the stent cell geometry. These parameter studies are performed for the four different values of mismatch ΔM . The smallest value $\Delta M = 1.6$ (mm) is such that the diameter D of the expanded stent is smaller than the lumen diameter of the healthy arterial region \bar{L} , while for the largest value of mismatch $\Delta M = 4.6$ (mm) the diameter D is larger than \bar{L} , and the stent over-stretches the artery significantly. In order to compute parameter D_2 we have used the assumptions that $\Delta\sigma_I = 0$ and $w_2 = 0$, which refer to eqs. (3) and (4).

For each numerical simulation, the scalar indicators LG , D_1 and D_2 were computed on the basis of 945 and 3150 3D-elements. If the resulting scalars varied less than 3%, then the results were accepted. If this was not the case, then the simulations were repeated with the mesh consisting of 9765 3D-elements. It turned out that this additional refinement leads to deviations less than 3% for all scalar indicators with respect to the coarser mesh.

3.1 Influence of mismatch ΔM

In the first parameter study, which will serve as the basis for the additional simulations, we have computed the influence of the important mismatch ΔM on the intimal pressure concentration caused by the stent struts D_1 , the stress change within the arterial wall caused by the stent D_2 , and the lumen gain during stenting LG . This study was performed for the three different stent geometries S1, S2, S3 illustrated in Fig. 2.

The resulting data points are registered in diagrams comparing the influence of the mismatch ΔM and the different stent geometries on the indicators D_1 , D_2 , LG . The finite element results

are illustrated in Fig. 5 by solid lines with different weights, and denoted as ‘original strut thickness’ (abbreviated by ‘orig st’). In this figure and in all following figures we indicate a particular value of mismatch ΔM for a specific stent by a circle, which is filled or partly filled. For example, a circle filled up by a quarter indicates the mismatch $\Delta M = 1.6$ (mm).

3.2 Influence of strut thickness

The dimension of a strut, which is in contact with the arterial wall, has a strong effect on changes in the intimal pressure concentration, stress changes in the arterial wall and the lumen gain after stenting. It also effects significantly the clinical outcome after stenting [25], [27]. Note that the strut thickness s_t is mainly responsible for the stiffness of the stent, while the strut width s_w changes the contact pressure between the strut and the (intimal) surface.

In this section we illustrate the numerical results obtained from studies, which use (i) a reduced strut thickness for the entire stent, and (ii) a reduced strut thickness only for the end cells of the stent.

3.2.1 Reduction of strut thickness for the entire stent

The entire study of Section 3.1 was repeated with just a half of the stent strut thickness for all stents. The finite element meshes and all other geometrical data are as above. Hence we used $s_t = 225$ (μm) for S1, S2 and S3. The results are illustrated in Fig. 5 by dashed lines with different intensities, and denoted as ‘half strut thickness’ (abbreviated by ‘half st’). They compare the influence of the mismatch ΔM and the different stent geometries on D_1 , D_2 , LG .

3.2.2 Reduction of strut thickness for the end cells of the stent

For all investigated stent designs we parameterize the strut thickness s_t of the cells at both ends of the stent, i.e. for region d , see Fig. 6. In particular, for these end regions we have reduced s_t to 50% of its original value ($s_t = 225$ (μm)), and have repeated the entire study with the finite element meshes and all other geometrical data, as used in Section 3.1. Since the effect of this modification will mainly occur around the stent ends, we have only considered the regions around the stent ends for the computation of the indicators D_1 , D_2 , LG , according to

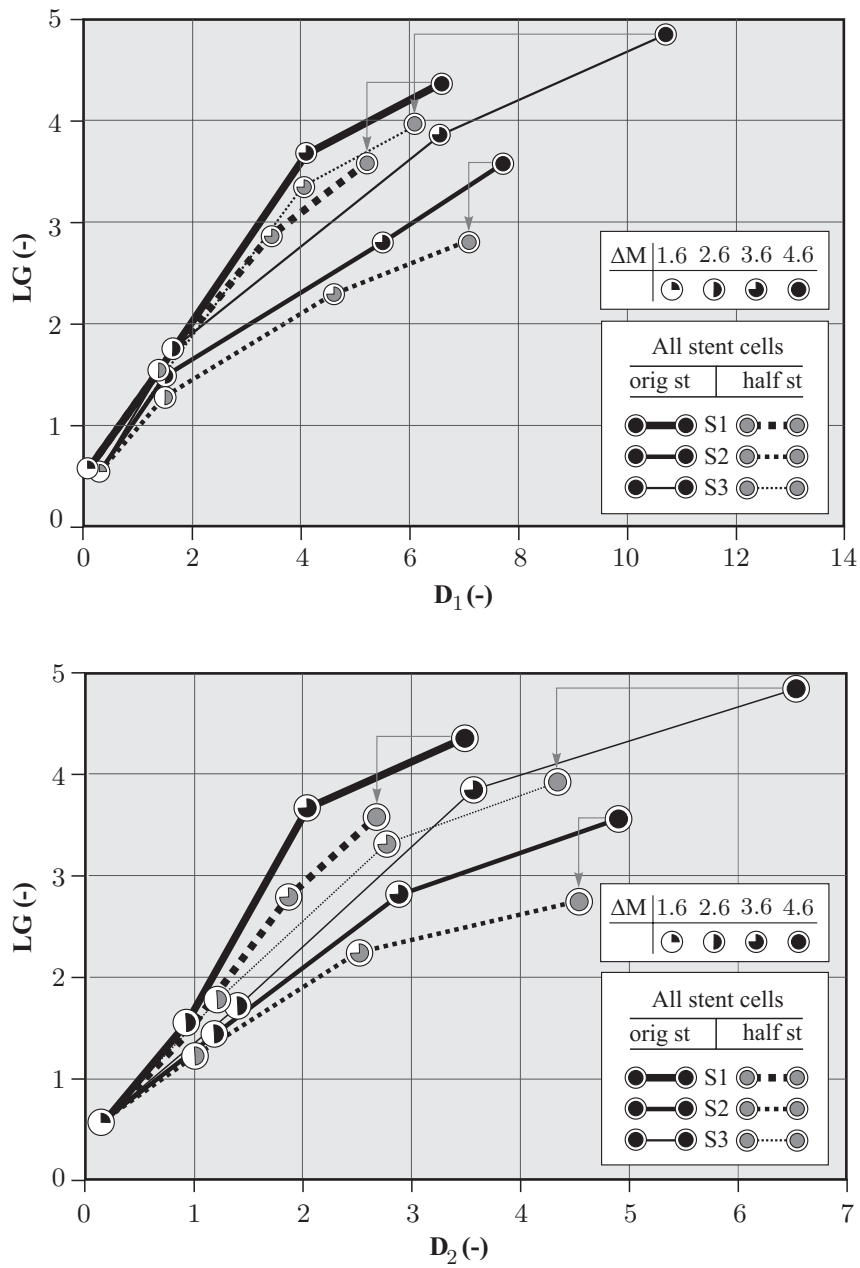


Figure 5: Influence of mismatch $\Delta M = D - M$ and the different stent geometries S1, S2, S3 on the three indicators D_1 , D_2 , LG . Solid lines indicate the ‘original strut thickness’ (orig st). Dashed lines indicate the results obtained by reducing the strut thickness for the entire stent by a half (half st). A particular value of mismatch for a specific stent is indicated by a circle, which is filled or partly filled. For each stent type, arrows indicate the change from ‘orig st’ to ‘half st’-data at $\Delta M = 4.6$.

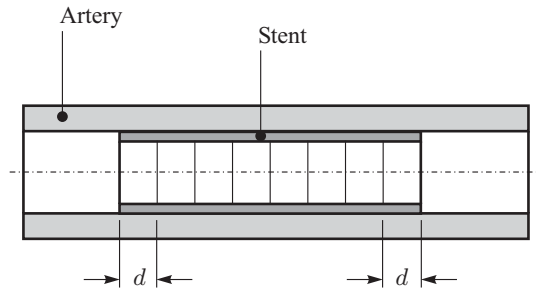


Figure 6: Cells at both ends of the stent, indicated by the dimension d (see Fig. 2), in which the strut thickness s_t is reduced to 50% of its original value ($s_t = 225 \text{ } (\mu\text{m})$). Finite element meshes and geometrical data for all other cells remain at their original values.

eqs. (1), (4), (6), respectively. In particular, the finite elements considered for the analysis of the edge effects are from the inside of the dotted frames defined in Section D-D of Fig. 1. This approach makes the effect of the variation of the strut thickness better visible in the diagrams. The numerical results are shown in Fig. 7, where solid lines indicate the ‘original strut thickness’ (‘orig st’), and dashed lines the results obtained by reducing the strut thickness for the end cells of the stent by a half (abbreviated by ‘half st’).

3.3 Influence of cell geometry

Finally, numerical results are presented by uniformly modifying the geometry of the cells throughout the stent illustrated in Fig. 2 (for a non-uniform modification see the discussion in [33] and [50]). We have compared the influence of the mismatch ΔM and the modified stent geometries of S1, S2, S3 on the indicators D_1 , D_2 , LG . In particular, we have increased the original value d of all stent cells by 30% and set the number of cells m in the axial direction to $m = 6$ for S1, and $m = 5$ for S2 and S3. The numerical results are shown in Fig. 8, where solid lines indicate the ‘original cell geometry’ (‘orig cg’) for the stents S1, S2, S3, and the dashed lines are the results obtained by modifying the geometry of all cells of the stent as described above (abbreviated by ‘modif cg’).

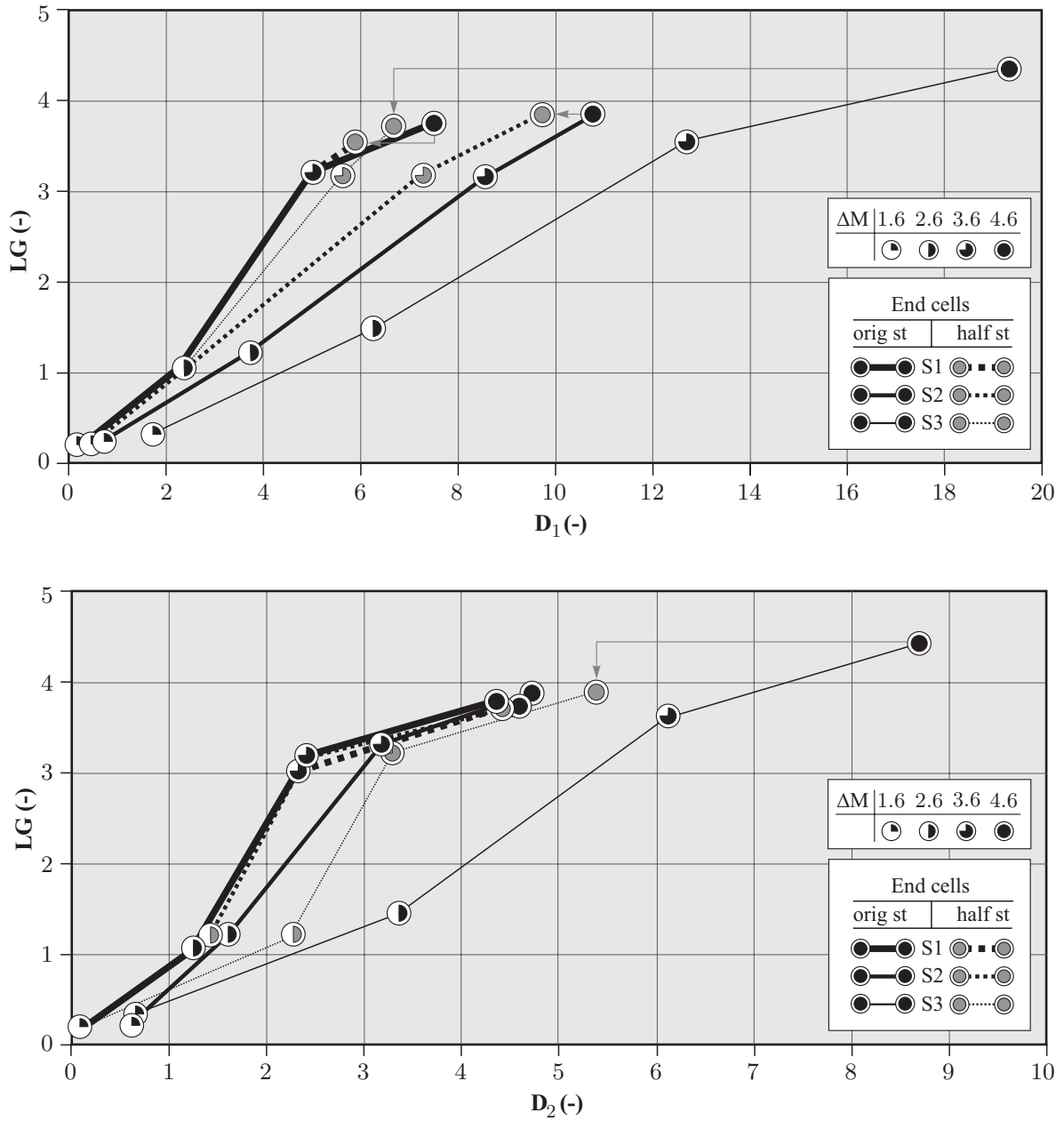


Figure 7: Influence of mismatch $\Delta M = D - M$ and the different stent geometries S1, S2, S3 on the three indicators D_1 , D_2 , LG . Only the finite elements inside the dotted frames, as defined in Section D-D of Fig. 1, were considered for the computation of the indicators. Solid lines indicate the ‘original strut thickness’ (orig st), as in Fig. 5. Dashed lines indicate the results obtained by reducing the strut thickness for the end cells of the stent by a half (half st). For each stent type, arrows indicate the change from ‘orig st’ to ‘half st’-data at $\Delta M = 4.6$.

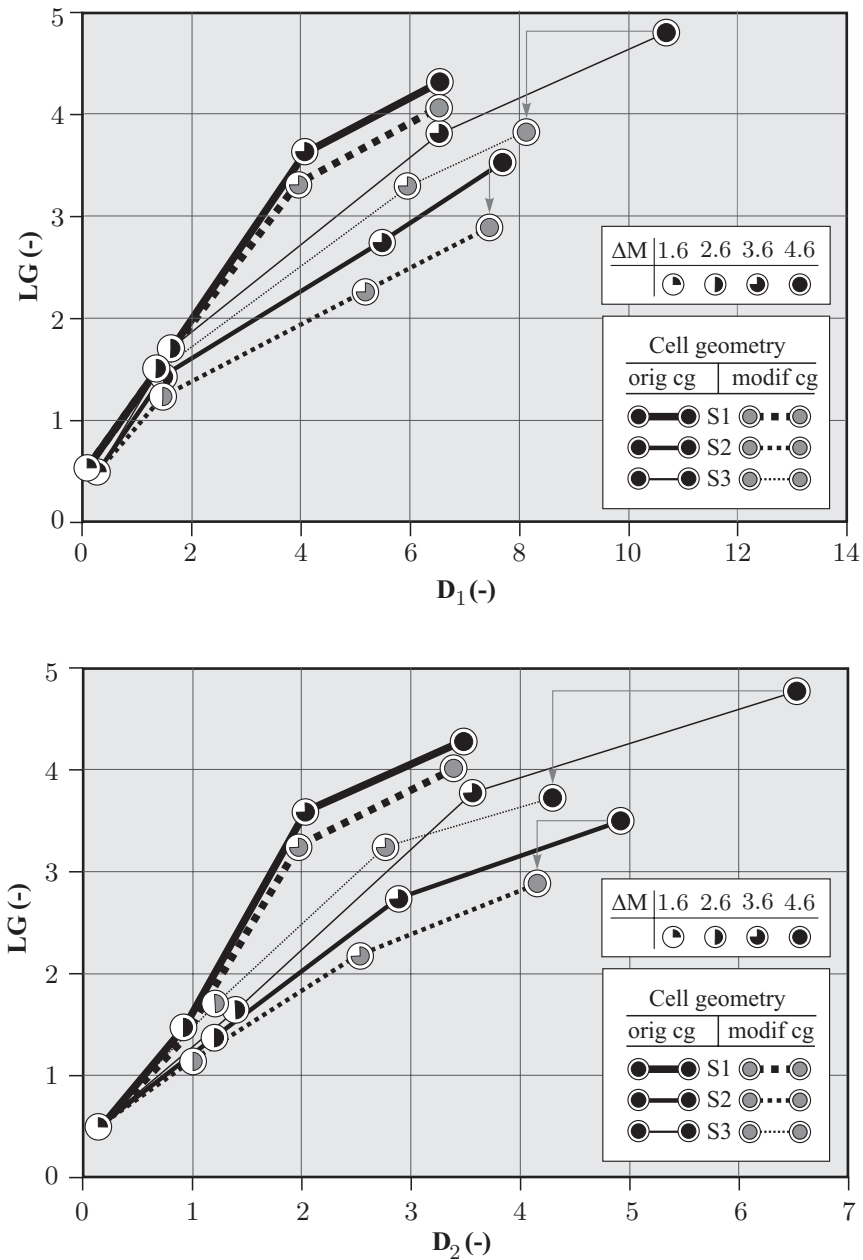


Figure 8: Influence of mismatch $\Delta M = D - M$ and the modified geometries of stents S1, S2, S3 on the three indicators D_1 , D_2 , LG . Solid lines indicate the ‘original cell geometry’ (orig cg), as in Fig. 5. Dashed lines indicate the results by modifying the cell geometry (modif cg). The original width d of all stent cells (see Fig. 2) is increased by 30%. For each stent type, arrows indicate the change from ‘orig cg’ to ‘modif cg’-data at $\Delta M = 4.6$.

4 Discussion

Three-dimensional finite element simulations of these nature produce, in general, a high amount of numerical stress and strain data, which to interpret is not a straightforward task. For this reason we have introduced three (scalar) indicators D_1 , D_2 and LG , which provide a measure for the quality of a performed angioplasty procedure by comparing the mechanical situation before the treatment with that after. Hence, these indicators attempt to characterize the change of the three-dimensional mechanical situation due to angioplasty by scalar values. In particular, the values of the indicators D_1 and D_2 are measures for the intimal pressure concentration and the stress change within the arterial wall caused by the stent, respectively. Hence, it is reasonable to assume that the lower the values D_1 and D_2 (with $w_2 = 0$) are for the same achieved lumen gain LG and mismatch ΔM , the lower is the risk of damage in the tissue components, and, consequently, the better is the treatment and the selected stent. It is certainly a tradeoff between D_1 , D_2 and the lumen gain LG to judge if the used stent is optimal or not. To decide, which indicator is the most important one for optimization procedures depends on the specific patient and the related patient history.

With these indicators we performed parametric studies of (i) the strut thicknesses for the entire stent, (ii) the strut thicknesses for the end cells of the stent with dimension d , and (iii) the stent cell geometry. The studies were performed for each of the three stents and for four mismatches ΔM defined to be the difference between the diameter of the expanded stent and smallest lumen diameter in the stenosis before angioplasty.

General observations of the obtained numerical results indicated in Figs. 5, 7, 8 are as follows: there seems to be a global tendency of the indicators D_1 and D_2 to increase faster in the region of larger values of LG than in the region of smaller values of LG . In addition, one would possibly expect that all the curves in Figs. 5, 7, 8 start from the origin. For mismatches ΔM below a certain (small) limit, the stent does not interact with the entire lumen surface after full expansion, when the lumen surface is elliptically shaped, which is the case in the present study. Hence, there is lumen gain LG accompanied with a (very) small change in the mechanical environment. For values above a certain limit of ΔM (here about 1.5) the expanded stent interacts then with the entire lumen surface and then effect the indicators D_1 and D_2 . For all our studies

we have fixed the metal-to-artery ratio to 0.15 at the nominal diameter D . If for some reason the metal-to-artery ratio decreases with increasing ΔM , then the values of D_1 would be larger than in the present study, and *vice versa*.

Referring to Fig. 5, for all values of mismatch ΔM the use of stent S3 (InFlowTM-Gold-Flex) leads to the largest and S1 (Multi-Link-TetraTM) to the lowest values of D_1 and D_2 . It is interesting to relate this result to the clinical study documented in [26], which has shown a high restenosis rate of 50.3% for stent S3, and a low restenosis rate of 20.0% for stent S1. In addition, stent S1 gives almost the same lumen gain as S3, but much less change in the mechanical environment of the arterial wall expressed through D_1 and D_2 . For example, for $\Delta M = 4.6$ (mm), stent S1 induces only about half the stress, which is induced by stent S3, whereby S1 achieves approximately 90% of LG of S3. For any fixed value ΔM , stent S3 has the largest lumen gain LG when compared with stents S1 and S2.

The dashed lines in Fig. 5 indicate the results obtained by reducing the strut thickness for the entire stent by a half. Thereby, for all stents, the effect of this change becomes more apparent with increasing mismatch ΔM . The largest mechanical change in the arterial wall is observed for stent S3 at a mismatch $\Delta M = 4.6$. Remarkably, as can be seen from Fig. 5, by reducing the strut thicknesses of the entire stent S3 by 50% it performs similar to stent S1, at least for the $LG-D_1$ ratio. The least advantageous effect of changing the thickness of the struts is achieved for stent S1 at $\Delta M = 3.6$; D_1 and D_2 are almost unchanged, while LG decreases significantly, which is an obvious disadvantage.

The studies, documented in [25], [27], compared the angiographic result of two different stent products related to either the ‘thin-strut’ group or to the ‘thick-strut’ group, depending on the strut thickness s_t . In particular, [25] compared the ACS RX Multi-LinkTM stent, with $s_t = 50$ (μm) and $s_w = 100$ (μm) (‘thin-strut’ group), to the ACS Multi-Link RX DuetTM stent, with $s_t = 140$ (μm) and $s_w = 100$ (μm) (‘thick-strut’ group). Both stents were manufactured by the same company (Guidant/Advanced Cardiovascular Systems). It was shown that the incidence of angiographic restenosis was reached in 15% of the thin-strut stent patients and 25.8% of the thick-strut stent patients, which corresponds to a risk reduction of 42%. The study [27] compares the ACS RX Multi-LinkTM stent (Guidant) to the BX VelocityTM stent (Cordis Corp.), with $s_t = 140$ (μm) and $s_w = 100$ (μm), (‘thick-strut’ group). This study has shown

that the incidence of angiographic restenosis is 17.9% in the ‘thin-strut’ group and 31.4% in the ‘thick-strut’ group.

Both studies point out that the stent with thinner struts elicits less angiographic restenosis than the thicker-strut stent. From Fig. 5 we read that thinner struts lead to a decrease in the values D_1 and D_2 (with $w_2 = 0$), and hence to a decrease in the intimal pressure concentration and the stress change within the arterial wall due to the stent, which produce less local damage. However, we also learn from Fig. 5 that stents with thinner struts also lead to less lumen gain LG due to stenting since thinner struts reduce the overall stiffness of the stent. Note that this important parameter was not analyzed and discussed in the studies [25], [27].

Evidence is emerging that the abrupt compliance mismatch, which occur at the junction between both ends of the stent and the host arterial wall, disturbs the vascular hemodynamics and the natural wall stress distribution [50]. In particular, the stress distributions show peaks close to both ends of the stent due to the phenomenon of ‘dog-boning’ or ‘dumb-belling’ of the stent, analyzed numerically in, for example, [30]. The phenomenon of ‘dog-boning’ might be avoided by (i) using a shaped balloon, (ii) varying the geometry of the stent cells over the stent length, or (iii) varying the thickness of the struts in certain areas of the stent [33]. In [50], approach (ii) was chosen to design compliance matching stents. Although approach (iii) seems to be difficult for producing appropriate stent devices [33], some manufacturers have started to create stents with variable thickness struts. One example is the VTSTM(Variable Thickness Strut) technology of Guidant which is designed to provide enhanced flexibility, deliverability, and surface area coverage while maintaining radial strength. Therefore, in our study we have chosen approach (iii). Figure 7 shows the influence of the mismatch and the different stent geometries on the three indicators D_1 , D_2 , LG when the strut thickness for the end cells of the stent is reduced by a half (dashed lines). It turns out that the largest improvement regarding D_1 and D_2 is achieved for stent S3, and the smallest improvement is achieved for stent S1.

Another possibility to change the structure of a stent is by changing the cell geometry, while keeping the strut thickness. Figure 8 shows the results obtained from modified cell geometries (dashed lines). Hence, by comparing the study, which uses half of the strut thickness for the entire stent (dashed lines in Fig. 5), with the study, which is based on modified cell geometries (Fig. 8) we learn that stents S2 and S3 behave very similar under both modifications. However,

for stent S1 this is not true. When comparing the outcome of stent S3, it reveals that D_1 is reduced more effectively with the use of a uniform strut thickness variation than a uniform cell geometry variation. Still, the other indicators LG and D_2 are changed similarly by both methods. Consequently, a strut thickness variation is preferable for S3.

4.1 Study limitations

To outline the methodology of computing appropriate scalar measures used to characterize the ‘quality’ of the angioplasty treatment we have used a human high-grade stenotic iliac artery for which we have had available a complete set of geometrical and mechanical data. Iliac arteries are much bigger than, for example, coronary arteries, and hence they are easier to access, to separate into the individual tissue components, and to test. The current (clinical) research focuses, however, mainly on intracoronary stenting and optimization procedures of stent designs for the coronary site. Since we wanted to discuss our numerical results obtained for different stent types with clinical studies and related issues of restenosis we have used here stent types, which are employed for coronary angioplasty. In addition, since we are not aware of the specific composition of the (shape memory) alloys for the investigated stents the material responses of all stents were assumed to be the same as for stainless steel. Since we used an iliac artery model, while coronary stents and results from coronary stent clinical trials are used in the interpretation of the results, and since the three investigated stent types differ in material and related mechanical property, we can not draw conclusions about a real stent product. Hence, improved simulations are then based on improved constitutive equations and geometrical data for the stents and on the morphology of a patient-specific stenotic coronary artery. In order to assess the suitability of real stent products, one has to perform simulations within their actual working environment. A variation of the stent length also seems to be a meaningful supplement to the present study.

Micro-damage and damage mechanism, which occur in the arterial wall due to vascular injury during stent deployment, have not been addressed in this study. In addition, balloon dilation frequently leads to tissue dissection within the intimal and/or medial layer and to plaque rupture. After balloon deflation this results in tissue flaps with longitudinal orientations protruding

into the vessel lumen [51]. Novel data of ultimate tensile stresses and stretches of the calcification and other tissue types obtained from nine human high-grade stenotic iliac arteries were recently reported in [39]. These data may serve to better model the biomechanics of atherosclerotic lesions. A first numerical approach to consider delamination processes of arterial tissue was recently proposed in [52].

Where it was possible, we compared our numerical results with clinical studies, and the agreement is satisfactory. Since the clinical studies have considered a large number of arteries, which differ from the one we have used, a direct comparison seems not to be feasible. In particular, due to a missing growth model, we are unable to specify a restenosis rate based on D_1 and D_2 . Instead, we can (only) provide a qualitative order of the restenosis rate in describing which stent may be more prone to restenosis than another, for a specific artery. Another factor which may be important, also neglected here, is the change in the wall-shear-stress (see, for example, [17], [18] among many others). This would require a flow simulation.

The proposed three indicators are normalized with respect to the situation in the diseased artery prior to stenting. Since clinicians judge the success of the procedure based on the nominal diameter of the healthy artery, an additional indicator determined with respect to a ‘normal’ situation would be meaningful to characterize the outcome of angioplasty; an important next step pursued in near future.

5 Conclusion

We have defined scalar indicators which allow a better judgement of the performance of stents used for a specific artery. Numerical studies allow the determination of changes of these indicators as a function of certain parameters such as stent cell type, geometry of stent strut and stent cell, and the mismatch between the smallest lumen diameter in the stenosis and the expanded stent diameter, a crucial parameter in clinical practice. The indicators are measures for the mechanical stresses produced during the expansion, which should be as small as possible, and for the lumen gain, which should be as large as possible.

The three-dimensional computational approach is based on numerical models for the arterial wall and the stent as well as on the stent-artery interaction. This combination seems to be a

step forward in the numerical modeling of balloon angioplasty. The numerical model for the investigated human iliac artery with a high-grade stenosis, which consists of eight different tissue types, is based on an approach previously documented [29], [30]. A specific anisotropic experimental data set at finite strains were adopted from [39]. The model also considers the axial *in situ* pre-stretch within the artery. In addition, we illustrated numerical models for three different stents which are based on products that are (or were) available commercially. The geometric structure of the different stents are parameterized to allow convenient changes. For the stent-artery interaction we have used an efficient contact algorithm [31].

Based on the investigated stenosis and the performed parameter studies it reveals that the best results for all three indicators can be achieved with stent S1, which has a similar structure as the Multi-Link-TetraTM stent. The worst results were achieved with stent S3, similarly structured as the InFlowTM-Gold-Flex stent, which is not available anymore on the market. In addition, the parametric studies reveal that certain modifications for one stent lead to more advantages than for another. For example, reducing the strut thickness by 50% in the end cells drastically reduces the values of the indicators D_1 and D_2 for stent S3 by almost keeping the value of the lumen gain LG , while it has almost no effect for stent S1.

It should be mentioned that the results may be (completely) different for other types of arteries, with other plaque composition and material properties, which can vary over orders of magnitude [39]. Although a general applicability of the results is not possible, a general applicability of the proposed methodology to computationally assess parametric stent designs is, however, possible. The methodology may provide clear markers for optimizing the treatment procedure, and the geometry and material of stent repeating-units, which may help stent designers to examine new stent designs on a ‘virtual’ patient before clinical trials.

Acknowledgements—The authors are indebted to Professor *R. Stollberger* from the division of clinical and experimental research for MR at Medical University Graz for his cooperation in developing appropriate MR sequences for high resolution plaque imaging. Thanks also go to *P. Regitnig, MD*, from the Institute for Pathology, Medical University Graz, for his support in harvesting autopsy specimens. Financial support for this research was provided by the *Austrian Science Foundation* under *START-Award Y74-TEC*. This support is gratefully acknowledged.

Appendix

Computation of the contact pressure $p_{j,\text{post}}$ and κ_j , as used in eq. (1)

For the evaluation of D_1 in eq. (1), the contact pressure $p_{j,\text{post}}$ for each finite element j is required. Due to the discrete nature of the finite element approach, the struts are only pointwise in contact with the (intimal) surface. For example, according to Fig. 9(a), a strut with length l_s is in contact with the surface through the nodal points 1 and 2, although the strut passes across seven finite elements. Hence, the discrete approach does not give any contact contribution to elements, which are not related with points 1 and 2, which is unlikely the case for real problems.

Therefore, we propose that the contact pressure between the stent strut and the (intimal) surface varies linearly from node 1 to 2. According to Fig. 9(a), we assume that several struts may cover a particular finite element j , which is part of the intimal surface. The algorithm for the computation of the pressure contribution of one strut to $p_{j,\text{post}}$ is as follows:

1. Compute the contact forces F_1 and F_2 at both ends of the strut (at nodes 1 and 2).
2. Compute the equivalent trapeziform distributed load q along the strut length l_s according to (see Fig. 9(b))

$$q = \sum_{I=1}^2 N_I q_I, \quad (9)$$

with the values $q_1 = 2(2F_1 - F_2)/l_s$ and $q_2 = 2(2F_2 - F_1)/l_s$ at nodes 1 and 2, respectively. Thereby, the shape functions N_I , $I = 1, 2$, have the simple forms $N_1 = 1 - x/l_s$ and $N_2 = x/l_s$.

3. Split the total strut length at the bounds of the finite elements into n_{el} strut segments (in Fig. 9, $n_{\text{el}} = 7$), and compute the length Δl_s^j of a strut segment, related to element j .
4. Finally, compute the contact pressure $p_{j,\text{post}}$ for element j as

$$p_{j,\text{post}} = \frac{\bar{q}_j}{s_w}, \quad \bar{q}_j = q|_{x=l_s^j}, \quad (10)$$

where, according to (9), \bar{q}_j is the contact force per unit length acting on element j , and s_w is the (constant) strut width, see Fig. 9(c). Length l_s^j is between $x = 0$ and the center of element j .

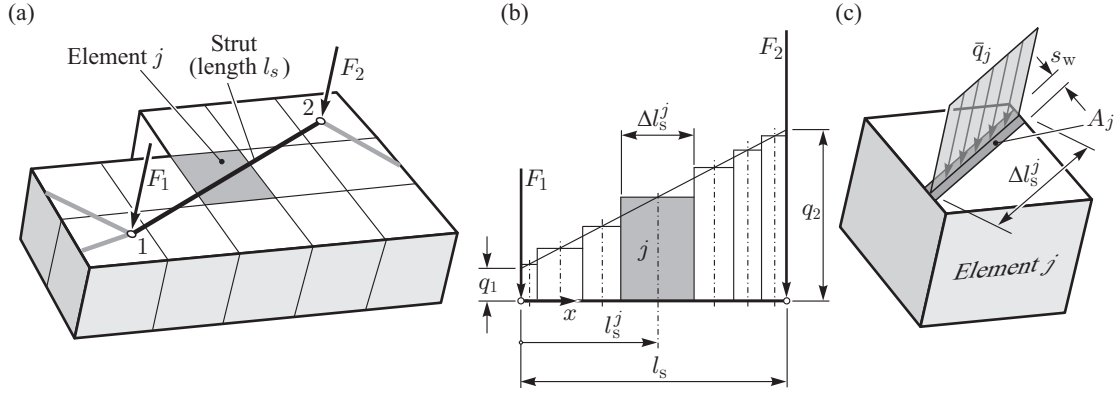


Figure 9: Computation of the contact pressure for a stent strut: (a) Intimal surface with contact forces F_1 and F_2 at both ends of the strut, (b) equivalent trapeziform distributed load along the strut length l_s , and (c) contact force \bar{q}_j per unit length acting on element j .

In eq. (1) the factor κ_j is determined according to

$$\kappa_j = \frac{A_j}{A_{el}}, \quad (11)$$

where A_j is the surface of element j , which is covered by the struts, and A_{el} is the surface area of the face of element j .

References

- [1] P. W. Serruys, P. de Jaegere, F. Kiemeneij, C. Macaya, W. Rutsch, G. Heyndrickx, H. Emanuelsson, J. Marco, V. Legrand, P. Materne, J. Belardi, U. Sijwart, A. Colombo, J. Goy, P. van den Heuvel, J. Delcan, and M. Morel. A comparison of balloon-expandable-stent implantation with balloon angioplasty in patients with coronary artery disease. Benestent Study Group. *New Engl. J. Med.*, 331:489–495, 1994.
- [2] D. L. Fischman, M. B. Leon, D. S. Baim, R. A. Schatz, M. P. Savage, I. Penn, K. Detre, L. Veltri, D. Ricci, M. Nobuyoshi, M. W. Cleman, R. R. Heuser, D. Almond, P. S. Teirstein, R. D. Fish, A. Colombo, J. Brinker, J. Moses, A. Shaknovich, J. Hirshfeld, S. Bailey, S. Ellis, R. Rake, and S. Goldberg. A randomized comparison of coronary-stent placement

- and balloon angioplasty in the treatment of coronary artery disease. Stent restenosis study investigators. *New Engl. J. Med.*, 331:496–501, 1994.
- [3] R. Erbel, M. Haude, H. W. Hopp, D. Franzen, H. J. Rupprecht, B. Heublein, K. Fischer, P. de Jaegere, P. Serruys, W. Rutsch, and P. Probst. Coronary-artery stenting compared with balloon angioplasty for restenosis after initial balloon angioplasty. Restenosis stent study group. *New Engl. J. Med.*, 339:1672–1678, 1998.
- [4] M. Hoher, J. Wohrle, O. C. Grebe, M. Kochs, H. H. Osterhues, V. Hombach, and A. B. Buchwald. A randomized trial of elective stenting after balloon recanalization of chronic total occlusions. *J. Am. Coll. Cardiol.*, 34:722–729, 1999.
- [5] R. S. Schwartz, K. C. Huber, J. G. Murphy, W. D. Edwards, A. R. Camrud, R. E. Vlietstra, and D. R. Holmes. Restenosis and proportional neointimal response to coronary artery injury: results in a porcine model. *J. Am. Coll. Cardiol.*, 19:267–274, 1992.
- [6] E. J. Topol. Caveats about elective coronary stenting. *New Engl. J. Med.*, 331:539–541, 1994.
- [7] D. Y. Leung, S. Glagov, and M. B. Mathews. Cyclic stretching stimulates synthesis of matrix components by arterial smooth muscle cells *in vitro*. *Science*, 191:475–477, 1976.
- [8] D. L. Wang, B. S. Wung, Y. J. Shyy, C. F. Lin, Y. J. Chao, S. Usami, and S. Chien. Mechanical strain induces monocyte chemotactic protein-1 gene expression in endothelial cells. Effects of mechanical strain on monocyte adhesion to endothelial cells. *Circ. Res.*, 77:294–302, 1995.
- [9] E. R. Edelman and C. Rogers. Hoop dreams: stents without restenosis. *Circ.*, 94:1199–1202, 1996.
- [10] J. G. Murphy, R. S. Schwartz, W. D. Edwards, A. R. Camrud, R. E. Vlietstra, and D. R. J. Holmes. Percutaneous polymeric stents in porcine coronary arteries. *Circ.*, 86:1596–1604, 1992.

- [11] C. Rogers and E. R. Edelman. Endovascular stent design dictates experimental restenosis and thrombosis. *Circ.*, 91:2995–3001, 1995.
- [12] A. König, T. M. Schiele, J. Rieber, K. Theisen, H. Mudra, and V. Klauss. Influence of stent design and deployment technique on neointima formation and vascular remodeling. *Z. Kardiol.*, 91:98–102, 2002.
- [13] D. R. McLean and N. L. Eiger. Stent design: implications for restenosis. *Rev. Cardiovas. Med.*, 3:16–22, 2002.
- [14] T. M. Sullivan, S. D. Ainsworth, E. M. Langan, S. Taylor, B. Snyder, D. Cull, J. Youkey, and M. Laberge. Effect of endovascular stent strut geometry on vascular injury, myointimal hyperplasia, and restenosis. *J. Vasc. Res.*, 36:143–149, 2002.
- [15] R. Hoffmann, G. S. Mintz, R. Mehran, K. M. Kent, A. D. Pichard, L. F. Satler, and M. B. Leon. Tissue proliferation within and surrounding Palmaz-Schatz stents is dependent on the aggressiveness of stent implanation technique. *Am. J. Cardiol.*, 83:1170–1174, 1999.
- [16] J. J. Wentzel, J. Kloet, I. Andhyiswara, J. A. Oomen, J. C. Schuurbiens, B. J. de Semet, M. J. Post, D. de Kleijn, G. Paterkamp, C. Borst, C. J. Slager, and R. Krams. Shear-stress and wall-stress regulation of vascular remodeling after balloon angioplasty: effect of matrix metalloproteinase inhibition. *Circ.*, 104:91–96, 2001.
- [17] A. Thury, G. van Langenhove, S. G. Carlier, M. Albertal, K. Kozuma, E. Regar, G. Sianos, J. J. Wentzel, R. Krams, C. J. Slager, J. J. Piek, and P. W. Serruys. High shear stress after successful balloon angioplasty is associated with restenosis and target lesion revascularization. *Am. Heart J.*, 144:136–143, 2002.
- [18] J. J. Wentzel, F. J. H. Gijssen, N. Stergiopoulos, P. W. Serruys, C. J. Slager, and R. Krams. Shear stress, vascular remodeling and neointimal formation. *J. Biomech.*, 36:681–688, 2003.
- [19] R. Fattori and T. Piva. Drug-eluting stents in vascular intervention. *Lancet*, 361:247–249, 2003.

- [20] M. Degertekin, E. Regar, K. Tanabe, P. C. Smits, W. J. van der Giessen, S. G. Carlier, P. de Feyter, J. Vos, D. P. Foley, J. M. Ligthart, J. J. Popma, and P. W. Serruys. Sirolimus-eluting stent for treatment of complex in-stent restenosis: the first clinical experience. *J. Am. Coll. Cardiol.*, 41:184–189, 2003.
- [21] J. J. Popma, M. Suntharalingam, A. J. Lansky, R. R. Heuser, B. Speiser, P. S. Teirstein, V. Massullo, T. Bass, R. Henderson, S. Silber, P. von Rottkay, R. Bonan, K. K. Ho, A. Ostattin, and R. E. Kuntz. Randomized trial of 90sr/90y beta-radiation versus placebo control for treatment of in-stent restenosis (start). *Circ.*, 106:1090–1096, 2002.
- [22] R. Waksman, A. E. Raizner, A. C. Yeung, A. J. Lansky, and L. Vandertie. Use of localised intracoronary beta radiation in treatment of in-stent restenosis: The INHIBIT randomised controlled trial. *Lancet*, 359:543–544, 2002.
- [23] W. R. Castaneda-Zuniga. Pathophysiology of transluminal angioplasty. In J. Meyer, R. Erberl, and H. J. Rupprecht, editors, *Improvement of Myocardial Perfusion*, pages 138–141. Martinus Nijhoff Publisher, Boston, 1985.
- [24] R. Hoffmann, G. S. Mintz, G. R. Dussaillant, J. J. Popma, A. D. Pichard, L. F. Satler, K. M. Kent, J. Griffin, and M. B. Leon. Patterns and mechanisms of in-stent restenosis. A serial intravascular ultrasound study. *Circ.*, 94:1247–1254, 1996.
- [25] A. Kastrati, J. Mehilli, J. Dirschinger, F. Dotzer, H. Schühlen, F.-J. Neumann, M. Fleckenstein, C. Pfafferott, M. Seyfarth, and A. Schömig. Intracoronary stenting and angiographic results: strut thickness effect on restenosis outcome (ISAR-STEREO) trial. *Circ.*, 103:2816–2821, 2001.
- [26] A. Kastrati, J. Mehilli, J. Dirschinger, J. Pache, K. Ulm, H. Schühlen, M. Seyfarth, C. Schmitt, R. Blasini, F. Neumann, and A. Schömig. Restenosis after coronary placement of various stent types. *Am. J. Cardiol.*, 87:34–39, 2001.
- [27] J. Pache, A. Kastrati, J. Mehilli, H. Schühlen, F. Dotzer, J. Hausleiter, M. Fleckenstein, F. J. Neumann, U. Sattelberger, C. Schmitt, M. Muller, J. Dirschinger, and A. Schömig. In-

- tracoronary stenting and angiographic results: strut thickness effect on restenosis outcome (ISAR-STEREO-2) trial. *J. Am. Coll. Cardiol.*, 41:1283–1288, 2003.
- [28] R. S. Schwartz and T. D. Henry. Pathophysiology of coronary artery restenosis. *Rev. Cardiovas. Med.*, 3, Suppl. 5:S4–S9, 2002.
- [29] G. A. Holzapfel, C. A. J. Schulze-Bauer, and M. Stadler. Mechanics of angioplasty: Wall, balloon and stent. In J. Casey and G. Bao, editors, *Mechanics in Biology*, New York, 2000. The American Society of Mechanical Engineers (ASME). AMD-Vol. 242/BED-Vol. 46, pp. 141–156.
- [30] G. A. Holzapfel, M. Stadler, and C. A. J. Schulze-Bauer. A layer-specific three-dimensional model for the simulation of balloon angioplasty using Magnetic Resonance imaging and mechanical testing. *Ann. Biomed. Engr.*, 30:753–767, 2002.
- [31] M. Stadler and G. A. Holzapfel. Subdivision schemes for smooth contact surfaces of arbitrary mesh topology in 3D. *Int. J. Numer. Meth. Engr.*, 60:1161–1195, 2004.
- [32] J. Stolpmann, H. Brauer, H.-J. Stracke, R. Erbel, and A. Fischer. Mechanical behavior of coronary stents: Practicability and limitations of finite element simulation of the dilation behavior. 2002. submitted.
- [33] F. Auricchio, M. Di Loreto, and E. Sacco. Finite-element analysis of a stenotic revascularization through a stent insertion. *Comput. Meth. Biomech. Biomed. Engr.*, 4:249–264, 2001.
- [34] F. Migliavacca, L. Petrini, P. Massarotti, S. Schievano, F. Auricchio, and G. Dubini. Stainless and shape memory alloy coronary stents: a computational study on the interaction with the vascular wall. *Biomech. Model. Mechanobio.*, 2004. in press.
- [35] C. Rogers, D. Y. Tseng, J. C. Squire, and E. R. Edelman. Balloon-artery interactions during stent placement: a finite element analysis approach to pressure, compliance and stent design as contributors to vascular injury. *Circ. Res.*, 84:378–383, 1999.

- [36] Y. Jiang, K. Kohara, and K. Hiwada. Association between risk factors for atherosclerosis and mechanical forces in carotid artery. *Stroke*, 31:2319–2324, 2000.
- [37] P. J. Prendergast, C. Lally, S. Daly, A. J. Reid, T. C. Lee, D. Quinn, and F. Dolan. Analysis of prolapse in cardiovascular stents: a constitutive model for vascular tissue and finite element analysis. *J. Biomech. Engr.*, 125:692–699, 2003.
- [38] I.-K. Jang, G. Tearney, and B. Bouma. Visualization of tissue prolapse between coronary stent struts by optical coherence tomography. Comparison with intravascular ultrasound. *Circ.*, 104:2754, 2001.
- [39] G. A. Holzapfel, G. Sommer, and P. Regitnig. Anisotropic mechanical properties of tissue components in human atherosclerotic plaques. *J. Biomech. Engr.*, 2004. in press.
- [40] H. C. Stary. *Atlas of Atherosclerosis: Progression and Regression*. The Parthenon Publishing Group Limited, Boca Raton, London, New York, Washington, D.C., 2nd edition, 2003.
- [41] G. A. Holzapfel, T. C. Gasser, and R. W. Ogden. A new constitutive framework for arterial wall mechanics and a comparative study of material models. *J. Elasticity*, 61:1–48, 2000.
- [42] A. Delfino, N. Stergiopoulos, J. E. Moore Jr., and J.-J. Meister. Residual strain effects on the stress field in a thick wall finite element model of the human carotid bifurcation. *J. Biomech.*, 30:777–786, 1997.
- [43] G. A. Holzapfel, G. Sommer, and T. C. Gasser. Constitutive equations for the anisotropic mechanical response of tissue components in human atherosclerotic plaques.
- [44] C. A. J. Schulze-Bauer, C. Mörth, and G. A. Holzapfel. Passive biaxial mechanical response of aged human iliac arteries. *J. Biomech. Engr.*, 125:395–406, 2003.
- [45] T. C. Gasser and G. A. Holzapfel. A rate-independent elastoplastic constitutive model for (biological) fiber-reinforced composites at finite strains: Continuum basis, algorithmic formulation and finite element implementation. *Comput. Mech.*, 29:340–360, 2002.

- [46] G. A. Holzapfel. Structural and numerical models for the (visco)elastic response of arterial walls with residual stresses. In G. A. Holzapfel and R. W. Ogden, editors, *Biomechanics of Soft Tissue in Cardiovascular Systems*, pages 109–184, Wien, 2003. Springer-Verlag. CISM Courses and Lectures No. 441, International Centre for Mechanical Sciences.
- [47] J. C. Simo and T. J. R. Hughes. *Computational Inelasticity*. Springer-Verlag, New York, 1998.
- [48] D. Evans, editor. *Preconditioned iterative methods (Topics in Computer Mathematics)*, volume 4. Taylor and Francis, London, 1994.
- [49] C. Dumoulin and B. Cochelin. Mechanical behaviour modelling of balloon-expandable stents. *J. Biomech.*, 33:1461–1470, 2000.
- [50] J. L. Berry, E. Manoach and C. Mekkaoui, P. H. Rolland, J. E. Moore, and A. Rachev. Hemodynamics and wall mechanics of a compliance matching stent: *in vitro* and *in vivo* analysis. *J. Vasc. Interv. Radiol.*, 13:97–105, 2002.
- [51] D. W. Losordo, K. Rosenfield, A. Pieczek, K. Baker, M. Harding, and J. M. Isner. How does angioplasty work? Serial analysis of human iliac arteries using intravascular ultrasound. *Circ.*, 86:1845–1858, 1992.
- [52] T. C. Gasser and G. A. Holzapfel. Geometrically non-linear and consistently linearized embedded strong discontinuity models for 3D problems with an application to the dissection analysis of soft biological tissues. *Comput. Meth. Appl. Mech. Engr.*, 192:5059–5098, 2003.

	Intima			Media		Adventitia
	I-nos	I-fc	I-fm	M-nos	M-f	A
μ (kPa)	46.777	13.980	110.3	19.021	21.533	6.623
k_1 (kPa)	9992.89	80.163	32780.367	21.045	1839.550	118.483
k_2 (-)	80.24	65.351	785.443	79.362	1919.620	373.381
ρ (-)	0.91	0.75	0.23	1.0	1.0	0.1
τ_0 (kPa)	450.0	—	—	70.0	—	—
h (-)	1.0	—	—	2500.0	—	—
φ ($^\circ$)	53.90	77.549	46.02	26.348	23.595	42.291
$r(S_{\theta\theta})$ (-)	0.994	0.988	0.999	0.998	0.903	0.972
$r(S_{zz})$ (-)	0.994	0.995	0.999	0.968	0.955	0.992
ϵ (-)	0.062	0.089	0.023	0.037	0.087	0.123

Table 1: Material parameters characterizing the elastic response μ , k_1 , k_2 , ρ , φ , and the inelastic response τ_0 and h , of the different arterial components. These parameters were obtained by fitting the constitutive model to the corresponding experimental data of a human high-grade stenotic iliac arteries, as documented in [39]. The considered arterial tissues are: non-diseased intima I-nos, collagenous cap I-fc, fibrotic intima I-fm at the medial border, non-diseased media M-nos, diseased fibrotic media M-f and adventitia A. The table also contains the linear correlation coefficients $r(S_{\theta\theta})$, $r(S_{zz})$ and a second ‘error measure’ ϵ of the model fits, which is according to [44], Eq. 9. The calcification I-c is modeled as a very stiff tissue with $\mu = 2.25$ (MPa), while the lipid pool I-lp is modeled as a nearly incompressible ‘butter-like’ solid with $\mu = 0.05$ (kPa).

	a	b	c	d	e	f	g	h	i	j	k	l
S1	0.0	•	0.0	•	$0.6d$	–	–	–	–	–	–	–
S2	$0.15d$	•	$0.27b$	•	–	–	–	–	–	–	–	–
S3	$0.3d$	•	$0.2b$	•	$0.77d$	$0.46d$	$0.61d$	$0.17b$	$0.42b$	$0.5b$	$0.69b$	$0.15d$

Table 2: Geometrical parameters a - k of the three different cell types S1, S2, S3, as illustrated in Fig. 2.

For each cell type two parameters (b and d) are given, indicated by the symbol •, while all other parameters are functions of these two.

	S1				S2				S3			
D	3.0	4.0	5.0	6.0	3.0	4.0	5.0	6.0	3.0	4.0	5.0	6.0
b	4.7	6.28	5.24	4.17	2.35	2.09	2.24	2.09	2.35	2.09	2.24	2.09
d	5.65				3.29				3.29			
m	7				7				7			
n	2	2	3	4	4	6	7	9	4	6	7	9

Table 3: Specific parameters for the three different cell types S1, S2, S3. Nominal stent diameter D , and two geometrical parameters b and d in millimeter. Numbers of cells in the axial direction m , and in the circumferential direction n .